Icarus 398 (2023) 115541

Contents lists available at ScienceDirect

Icarus

journal homepage: www.elsevier.com/locate/icarus

The formation and evolution of Pluto's Sputnik basin prior to nitrogen ice fill

C.A. Denton [a,*], G.J. Gosselin [a], A.M. Freed [a], B.C. Johnson [a,b]

[a] Department of Earth, Atmospheric, and Planetary Sciences, Purdue University, West Lafayette, IN, United States of America
[b] Department of Physics and Astronomy, Purdue University, West Lafayette, IN, United States of America

ARTICLE INFO

Keywords:
Cratering
Impact processes
Pluto

ABSTRACT

We simulate Sputnik Planitia (SP), Pluto's largest impact basin, from formation through cooling and relaxation prior to loading of the basin with N_2 ice. To assess potential conditions for Pluto's interior that permit the formation of an SP-like basin in terms of depth and diameter, we consider impacts into targets that possess a subsurface ocean with variable ice shell thicknesses and thermal structures. We use a shock physics code to model excavation and transient crater collapse. Then, using the final temperature and density structure from the shock physics code as initial conditions, we simulate the subsequent cooling and viscoelastic relaxation of basin topography using a finite element model (FEM). We show that a thin ice shell (on the order of 100 km) overlying a thick ocean (on the order of 228 km) produces an SP-like basin in terms of diameter and pre-N_2 depth. A basin formed in a much thicker ice shell (200 km) overlying a thin ocean (128 km) can reproduce SP if the ice shell is relatively warm and possesses a strong rheology. Our results suggest that SP was not a mascon basin prior to subsequent loading by N_2 ice, but rather close to isostatically compensated. We find that SP could have developed into a mascon basin following N_2 loading if the ice shell is thin, conductive and possesses a lithosphere capable of supporting the N_2 load.

1. Introduction

The Sputnik Planitia (SP) basin is Pluto's largest putative impact basin at 1400 × 1200 km (McGovern et al., 2021), and is centered near the Pluto-Charon tidal axis (Nimmo et al., 2016). Its large size, location, and relationship to extensional tectonic features has led researchers to suggest that it induced planetary reorientation following the formation of a positive mass anomaly (mascon) (Keane et al., 2016; Nimmo et al., 2016). The evolution of SP into a mascon basin is hypothesized to originate from uplift of a subsurface ocean in conjunction with flexural loading by N_2 ice (Keane et al., 2016; Nimmo et al., 2016).

The interpretation of SP as a mascon basin has served as circumstantial evidence in favor of a potentially long-lived subsurface ocean on Pluto in conjunction with the expression of widespread extensional tectonics and the lack of a fossil bulge in Pluto's shape (Keane et al., 2016; Nimmo et al., 2016; Nimmo et al., 2017). However, the New Horizons flyby could not provide the gravity data necessary to derive constraints on Pluto's interior structure and its evolution over time. Fundamental characteristics of Pluto's interior at the time of SP's formation, including the presence and thickness of an ocean as well as the rheology and thermal structure of the overlying ice shell, remain poorly understood. As giant impact basins are known to reflect the thermal and mechanical structure of their target bodies at the time of formation (e.g., Ivanov et al., 2010), one means to improve our conceptual models of Pluto is to numerically simulate the origin and evolution of SP.

Here, we apply the modeling approach used to investigate the formation and evolution of lunar basins (Melosh et al., 2013; Freed et al., 2014; Trowbridge et al., 2020) by employing sequential numerical modeling to simulate the entirety of impact basin formation and evolution, from excavation and transient crater collapse through subsequent cooling and isostatic adjustment. Our objective is to assess the range of plausible conditions that persisted in Pluto's interior at the time of basin formation. Because the interior structure of Pluto is not well constrained at the time of impact, we consider the most critical characteristics that exert control on resulting basin morphology: the pre-impact thickness of Pluto's ice shell and subsurface ocean, and the thermal state of the ice shell. Following impact, we further assess the influence of ice rheology on final basin/ice shell morphology to better explore SP's evolutionary pathway prior to N_2 loading.

* Corresponding author.
E-mail address: adeened@arizona.edu (C.A. Denton).

https://doi.org/10.1016/j.icarus.2023.115541
Received 29 November 2022; Received in revised form 21 February 2023; Accepted 22 March 2023
Available online 28 March 2023

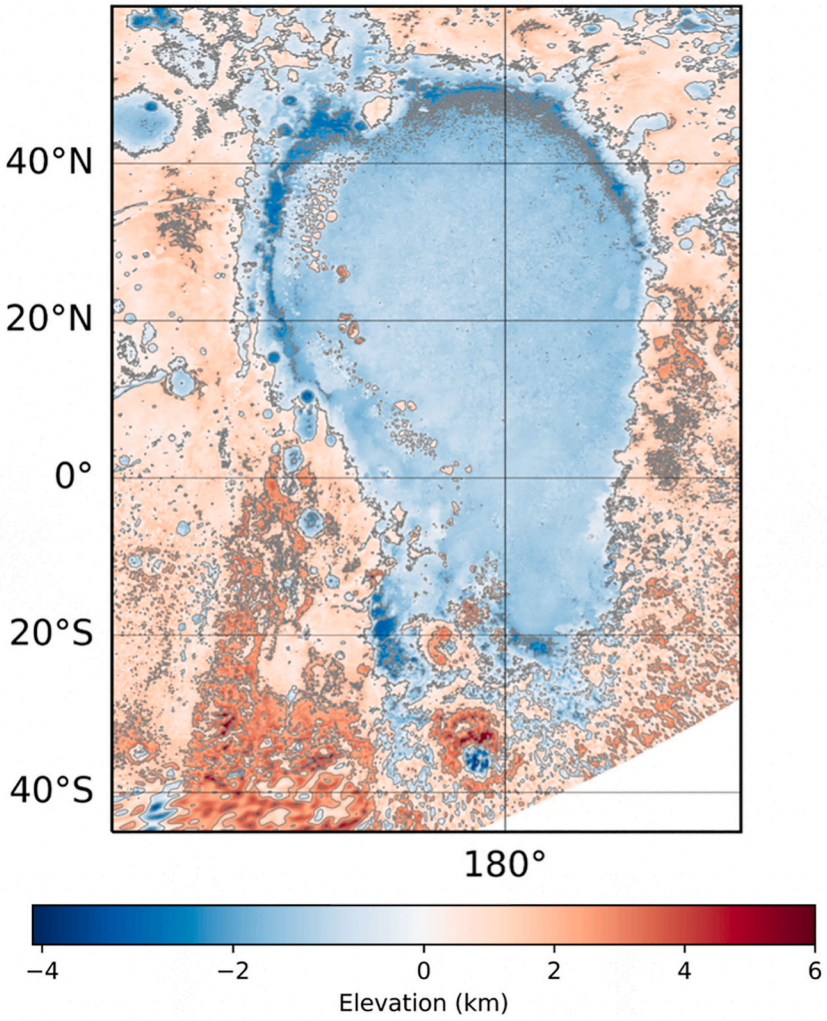

Fig. 1. Sputnik Planitia as captured in the global digital elevation model of Pluto (Schenk et al., 2018). Positive values (red) represent high elevation, while negative values (blue) represent low elevation relative to the geoid. Contours taken every kilometer. A broad ridge partially surrounds the central depression, which has been identified as the basin rim. The interior of the basin is filled with ~3–10 km of convecting N_2 ice and does not reflect the true topography of the basin floor. (For interpretation of the references to colour in this figure legend, the reader is referred to the web version of this article.)

2. Background

2.1. Sputnik Planitia

Following the New Horizons encounter, SP was initially estimated to be 800–1000 km in diameter (Stern et al., 2015; Nimmo et al., 2016). Schenk et al. (2018) subsequently identified a heavily eroded topographic rise ~125–175 km across surrounding the basin and re-defined SP as an elliptical basin with dimensions of 1200 × 2000 km, for an average basin diameter of ~1600 km. SP's rim rises ~1 km above the surrounding terrain and is degraded in many locations. It is poorly exposed along the basin's southern edge and has been extensively modified by impact cratering and glacial flow, limiting more accurate estimates of basin diameter (Schenk et al., 2018, Fig. 1). McGovern et al. (2021), using the most complete topographic data available, re-estimated the rim location such that the basin is slightly smaller: ~1300 km on average, a diameter which we aim to reproduce in our modeling.

The depth to the top of the N_2 ice occupying SP is estimated to be ~3 km (Schenk et al., 2018) and its thickness is estimated to be between 3 and 10 km (McKinnon et al., 2016; Trowbridge et al., 2016). This leads to an estimate of the depth of the empty basin to be between 6 and 13 km. Once flexural subsidence of the ice is considered, the estimated empty basin depth would be several km less, though quantifying this value is difficult since Pluto's elastic lithosphere is poorly constrained (Conrad et al., 2019; Mills and Montesi, 2019). A maximum depth of 10 km would be consistent with gravity scaling of basin depths on Iapetus (McKinnon et al., 2016).

Previous impact modeling used SP's formation to investigate Pluto's interior structure. Initial simulations used preliminary average estimates of basin diameter (~900 km) released by the New Horizons team (Moore et al., 2016) as an observational constraint and probed the influence of ice shell thickness and thermal structure on basin morphology and the possibility of mascon formation (Johnson et al., 2016). Johnson et al. (2016) found that a thick ocean (150 km) overlain by a 178-km ice shell produced an SP-like basin near isostatic equilibrium with an uplifted subsurface ocean beneath the basin, potentially compatible with mascon formation after loading by N_2 ice (Nimmo et al., 2016, Section 2.2). Subsequent impact modeling of SP (Denton et al., 2021) focused on impact-driven formation of antipodal terrain and assumed the larger average basin diameter of ~1600 km. These results concluded that reproduction of Pluto's antipodal terrain also necessitated the presence of a thick, 150-km subsurface ocean. However, neither investigation explored the influence of pre-impact thermal gradient on basin formation when Pluto's ice shell is entirely conductive, which is the now-dominant interpretation of Pluto's thermal structure (Nimmo et al., 2016; Kamata et al., 2019; Nimmo and McKinnon, 2021). Nor has any study used the post-collapse structure of SP from impact models as a means to self-consistently assess the role of cooling and isostatic adjustment on basin structure in the millions of years following formation, which may also alter the final state of the pre-N_2-filled basin significantly (e.g., Melosh et al., 2013; Freed et al., 2014). This

Table 1
Description of the iSALE model setup.

Description	Value
Size of high-resolution cell	2 km
Number of high-resolution cells, horizontal direction	600
Number of high-resolution cells, vertical direction	1050
Impact velocity	2 km/s
Surface gravitational acceleration	0.62 m s^{-2}
Target radius	1188 km
Core radius	860 km
Surface Temperature	44 K

Table 2
iSALE material input parameters.

Parameter description	Value for ice	Value for ocean	Value for dunite core
Equation of State	Tillotson ice	ANEOS water	ANEOS dunite
Poisson Ratio	0.33	NA	0.25
Cohesion (undamaged)	10 MPa	NA	5.07 MPa
Cohesion (damaged)	0.01 MPa	NA	0.01 MPa
Frictional coefficient (undamaged)	2.0	NA	1.58
Brittle ductile transition	689 MPa	NA	1.23 GPa
Tensile strength (undamaged)	0.17 MPa	NA	10 MPa
Melting temperature	Pressure-dependent	273 K	1373 K
Thermal softening parameter	1.2	NA	1.1
Acoustic fluidization decay time constant	36.4	NA	NA
Acoustic fluidization viscosity constant	0.523	NA	NA

investigation incorporates an exploration of ice shell thermal structure as well as thickness in numerical modeling of the entire evolution of the SP basin from impact, through crater modification, cooling, and isostatic adjustment, up until just prior to N_2 loading.

2.2. Mascon Basins

Mascon basins refer to the large, positive gravity anomalies associated with impact basins (the term mascon is short for mass-concentrations; Muller and Sjogren, 1968). Mascon basins are best characterized on the Moon, where they are distinct features in the lunar gravity field (e.g., Neumann et al., 1996). Both empty and mare-filled lunar mascon basins are observed. Empty mascon basins form when a lithospheric bridge forms during post-impact cooling between the basin center and the outer collar of thickened crust, enabling the former to be uplifted beyond an isostatic state as the latter rises due to isostatic forces (Melosh et al., 2013; Freed et al., 2014). Mare-filled mascon basins are formed by flexural support of the volcanic load, with modeling indicating that filled medium-sized basins (e.g., Humorum) were likely also mascons when empty (Freed et al., 2014). Larger basins such as South Pole-Aitken (SPA) do not form as mascon basins, as hydrostatic forces overwhelm lithospheric (flexural) strength, due to their larger size and greater post-impact temperatures (Trowbridge et al., 2020).

Sputnik Planitia as observed today (i.e., N_2-filled) has been argued to be a mascon basin on the basis of its location close to Pluto's tidal axis at the anti-Charon point (Keane et al., 2016; Nimmo et al., 2016; Nimmo and McKinnon, 2021). Such proximity is consistent with how planetary-scale positive mass anomalies reorient the body to align with the equator (e.g., the reorientation of the Tharsis volcanic rise on Mars, Citron et al., 2018). The previous lunar study of SPA (Trowbridge et al., 2020) suggests that SP was likely too large to have formed into a mascon basin during cooling and isostatic adjustment and did not become a mascon until it was loaded with dense N_2 ice (Nimmo et al., 2016; Keane et al., 2016; Johnson et al., 2016).

3. Modeling approach

Impact basin formation occurs on a vastly different timescale than subsequent cooling and viscoelastic relaxation associated with isostatic adjustment. Following Freed et al. (2014) and Trowbridge et al. (2020), we use a shock physics code to simulate the rapid process of basin excavation and collapse, which occurs in a matter of hours, followed by a finite element code, which captures the subsequent adjustment of the basin in response to conductive cooling and viscoelastic flow over the next tens of millions of years. This leads to a prediction of the final state of the basin (ice thickness, topography, and gravity signature) prior to N_2 ice fill for comparison to the constraints provided by New Horizons data and associated studies.

3.1. Impact modeling

We use the axisymmetric iSALE-2D shock physics code to simulate the initial basin-forming impact (Amsden et al., 1980; Collins et al., 2004; Wünnemann et al., 2006). We apply the inferred mean impactor velocity for Pluto of ~2 km/s (Zahnle et al., 2003), with a spherical target and realistic central gravity field that accounts for the influence of planetary curvature on basin morphology, necessary due the large size of the basin relative to the target body. Our model domain encompasses the entirety of Pluto as well as 1000 km above the target surface to adequately capture the large central uplift, with a spatial resolution of 2 km near the impact region that gradually increases with distance (Table 1).

We model impacts of an icy body into a spherical, three-layer Pluto-like target with pressure- and temperature-dependent densities according to appropriate equations of state: we use the Tillotson equation of state for the impactor and the ice shell (Bray et al., 2014), the ANEOS equation of state for water for the subsurface ocean (Turtle and Pierazzo, 2001), and the ANEOS equation of state for dunite for the core (Benz et al., 1989). To more accurately simulate the response of the ice shell to deformation, we use a full viscoelastic-plastic rheology to incorporate the potential contribution of viscous deformation during basin collapse (Johnson et al., 2016; Elbeshausen and Melosh, 2020). Ice shell strength and damage parameters are derived from fits to ice strength (Bray et al., 2014; Silber and Johnson, 2017). Core strength and thermal softening parameters come from fits to dunite rock strength (Davison et al., 2010; Potter et al., 2012). The ocean is considered to be a strengthless fluid. The material parameters used in iSALE are shown in Table 2.

In our models, we assess the effects of ice shell/ocean thickness and ice shell thermal structure on basin formation. We consider two structural scenarios: a thin, 100-km-thick ice shell, corresponding to a 228-km ocean, and a thick, 200-km-thick ice shell, corresponding to a 128-km ocean. These ice shell/ocean thicknesses encompass values similar to those found feasible in previous work (Johnson et al., 2016 and Denton et al., 2021, which favored a 178-km ice shell) and which are within bounds predicted by thermal evolution models (Bierson et al., 2020; Nimmo and McKinnon, 2021), as well as thin ice shells. Thinner (100-km) ice shells have been suggested in association with a thermally insulating methane clathrate layer (Kamata et al., 2019), and could further aid in production of a mascon in the basin. To isolate the influence of ocean thickness on resulting basin morphology, we hold constant both the radius of the core (860 km) and the combined ice shell/ocean thickness (328 km).

Pre-impact thermal structure is known to strongly influence impact basin morphology (e.g., Ivanov et al., 2010; Potter et al., 2012), and also dictates the magnitude of post-impact relaxation (e.g., Freed et al., 2014). Following Nimmo et al. (2016), we assume that the ice shell is entirely conductive, a limitation imposed by the necessity of sustaining large topographic variations over geologic time. We assume a nonlinear thermal structure for the ice shell (Johnson et al., 2017), which accounts

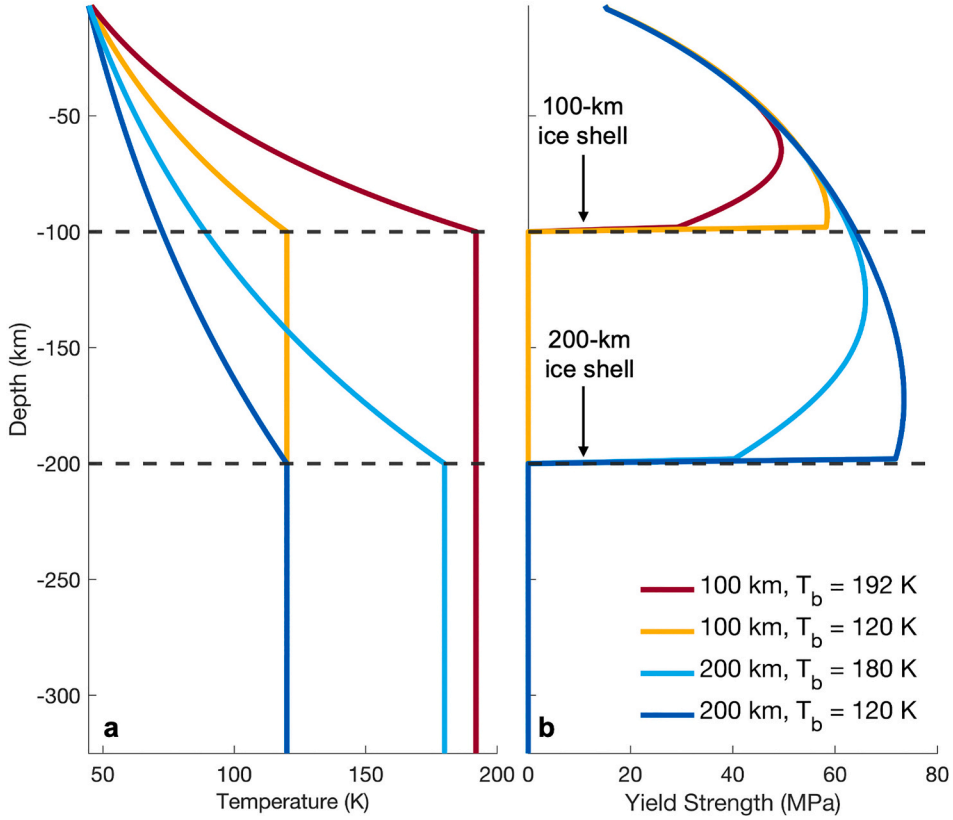

Fig. 2. (a) Thermal profiles used in iSALE simulations, labeled by their ice shell thickness and basal temperature (T_b); reference Table 3 for other notable parameters. (b) Corresponding pre-impact strength profiles associated with the evolution of temperature with depth. Dashed lines correspond to pre-impact ice shell thicknesses for thick and thin ice shells. Total depth plotted corresponds to the combined thickness of the ice shell and ocean (328 km).

Table 3
Description of models used.

Ice shell thickness (km)	Ocean thickness (km)	Basal temperature T_b (K)	Heat flux (mW/m^2)	Average thermal gradient (K/km)	Reference
100	228	192	9.73	1.48	Nimmo et al., 2016
100	228	120	6.59	0.76	Kamata et al., 2019
200	128	180	4.61	0.68	Nimmo et al., 2016
200	128	120	3.28	0.38	Kamata et al., 2019

for the linear dependence of ice's thermal conductivity with temperature. The resulting temperature profile as a function of depth is given by:

$$T(z) = T_s\left(\frac{T_b}{T_s}\right)^{\frac{z}{h_{cond}}} \quad (1)$$

where z is depth, T_s is the surface temperature, T_b is the basal ice shell temperature, and h_{cond} is the assumed thickness of the conductive portion of the shell, which we assume represents the entirety of the ice shell, consistent with previous work suggesting that Pluto's ice shell is entirely conductive (e.g., Nimmo and McKinnon, 2021).

We consider two thermal interpretations: the ice shell stays just warm enough to permit a liquid ocean (e.g., Nimmo et al., 2016; Bierson et al., 2020), or the ice shell is much colder than the underlying ocean in conjunction with an insulating methane clathrate layer (Kamata et al., 2019). Resulting thermal profiles for each of our four cases and their corresponding pre-impact yield strength profiles as a function of depth are shown in Fig. 2. For our 100-km ice shell, our thin, warm scenario uses a basal temperature of 192 K (Fig. 2), the warmest expected for a purely conductive ice shell (Nimmo et al., 2016). We consider a basal temperature of 120 K for our thin, cold ice shell following Kamata et al. (2019), which suggested basal temperatures 120–150 K may be feasible for 100–200 km-thick ice shells (Nimmo and McKinnon, 2021).

Our thick, warm ice shell uses a basal temperature of 180 K, the warmest expected for a 200-km conductive shell (Nimmo et al., 2016, Fig. 2). Our thick, cold ice shell follows our thin, cold shell and uses a basal temperature of 120 K (Fig. 2, Kamata et al., 2019). As noted in the strength profiles in Fig. 2b, while ice shell strengths are largely similar for the first ~50–75 km, the 200-km ice shells are much stronger than their 100-km counterparts. Fig. 2 illustrates how the yield strength changes with depth. Initially, strength increases with depth due to increases in pressure. The temperature of material also increases with depth, and as the melting temperature of ice is approached the strength decreases. We assume the ocean is strengthless, which results in a complete drop in strength at the ice-shell-ocean interface. The thermal and mechanical parameters for all scenarios studied are presented in Table 3.

Ocean temperature is assumed to be constant and equivalent to the temperature at the ice shell base for all thermal models; for a scenario with a cold ($T_b = 120$ K) ice shell, the presence of a clathrate layer would enable the ocean to be warmer than specified in the model.

3.2. Finite element modeling

We use the finite element code Abaqus to simulate the changes in

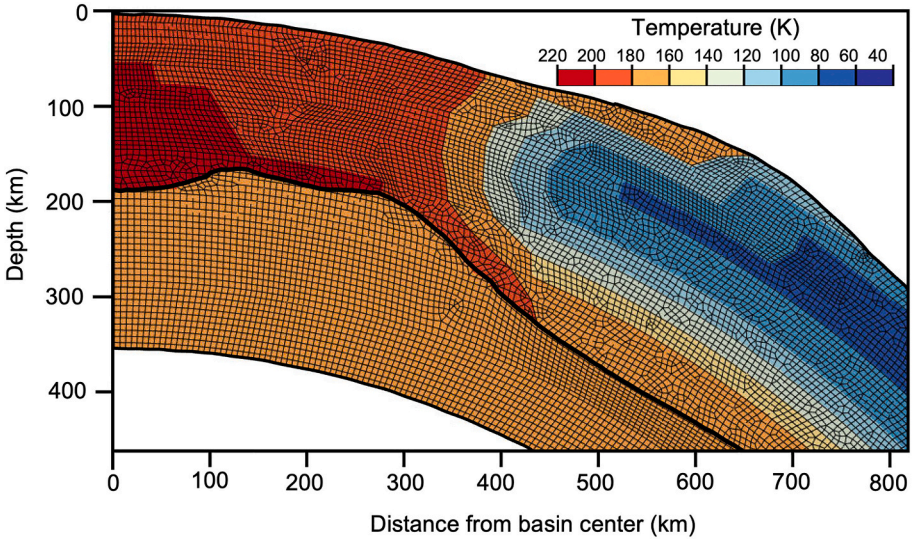

Fig. 3. Example of a high-resolution zone of a representative finite element model used in this analysis. Model shown is the post-impact thermal structure for the thick, warm ice shell to best exhibit ice shell thermal structure. Material colored according to temperature. Thin black lines represent the finite element mesh. Thick black lines correspond to material boundaries (top of ice shell, ice shell-ocean interface, base of ocean). The temperature structure shown is discussed in the results.

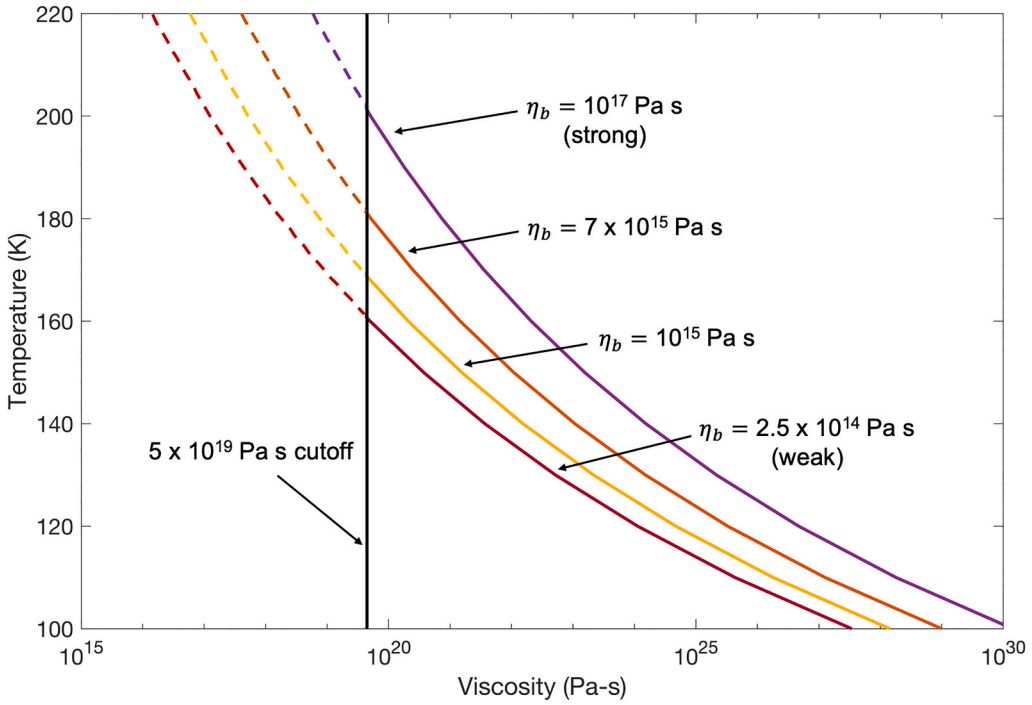

Fig. 4. Suite of major temperature-dependent ice viscosity models used in the FEM analysis. Viscosity profiles are defined using the formulation of Nimmo (2004). The reference viscosity (η_b) is identified for each example rheology. The 5×10^{19} Pa s cutoff is the minimum ice viscosity assumed for all models to prevent numerical instabilities (see text).

Table 4
Summary of results.

Ice shell (km)	Ocean (km)	T_b (K)	Cooling time	Post-impact depth (km)	Best-fit depth post-cooling (km)	Best-fit η_b used (Pa s)
100	228	192	70 Myr	9	10	Any
100	228	120	40 Myr	10	10.5	Any
200	128	180	175 Myr	12.5	7	7×10^{15}
200	128	120	150 Myr	18	14.5	2.5×10^{14}

basin morphology associated with conductive cooling and viscoelastic flow driven by isostatic adjustment. To maintain self-consistency within this two-code approach, each finite element model (FEM) uses initial conditions equivalent to the final steady-state geometry and thermal and density distributions from the corresponding impact simulation.

To match the shock physics code geometry, we use axisymmetric FEMs that incorporate planetary curvature and span half of Pluto, thus simulating the entirety of Pluto's ice shell and ocean. We do not model Pluto's core, as it does not contribute to post-impact basin adjustment because of the intervening weak ocean layer. We incorporate a high-resolution zone consisting of element sizes of ~6 km in the vertical

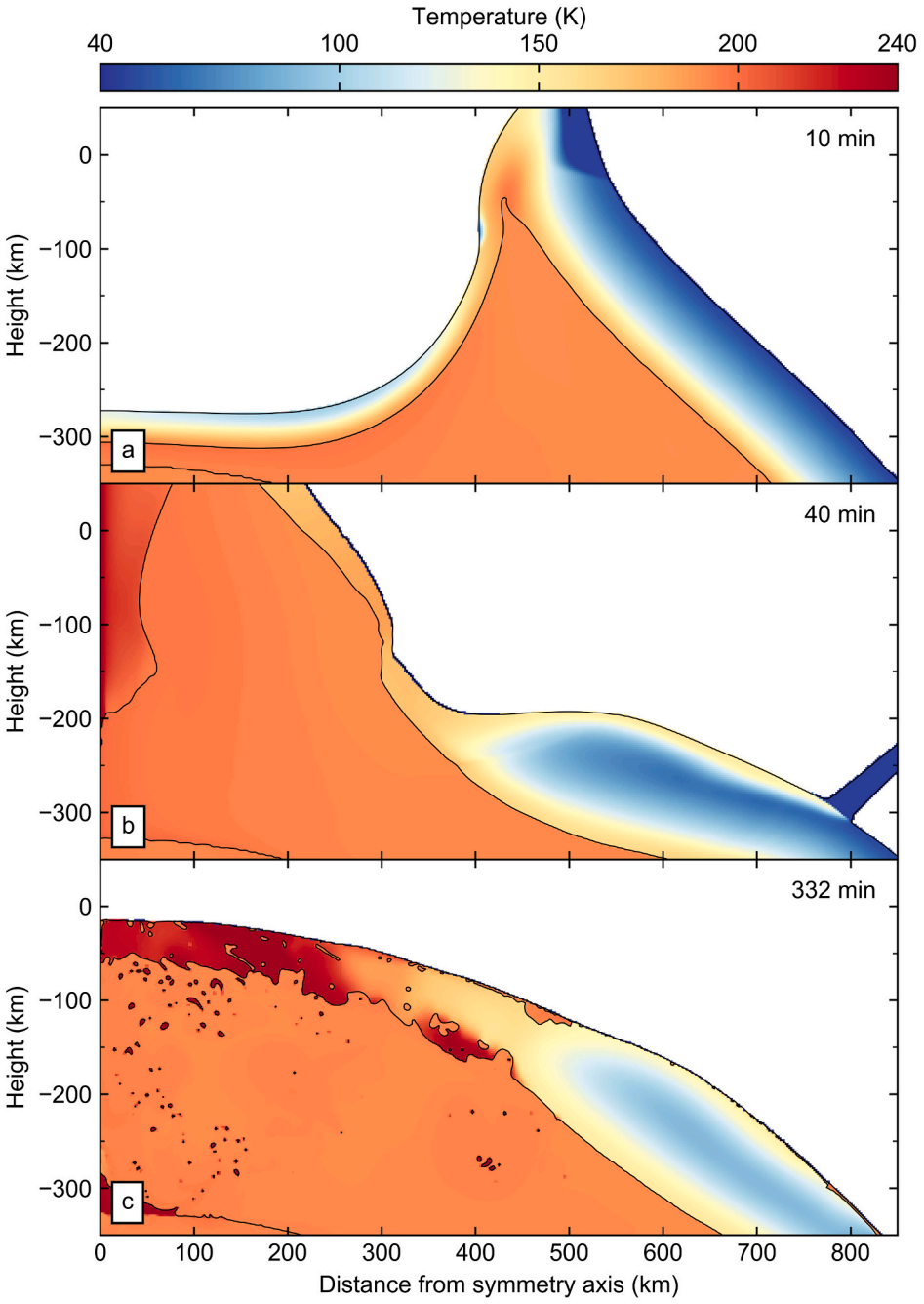

Fig. 5. Time series showing SP formation for our thin, warm ice shell scenario, which includes a 100-km-thick ice shell with a 192 K basal temperature, a 228-km-thick ocean and a 332-km-diameter impactor. Material colored according to temperature, which varies from the surface temperature (44 K) to elevated temperatures within the ice shell (240 K). Black curves mark material boundaries between core, ocean, ice shell, and void. Collision site is at the origin.

and horizontal directions, which extends from the symmetry axis in a 55-degree arc (1100 km from the basin center), the inner portion of which is shown in Fig. 3. Elements along the symmetry axis are assigned axisymmetric boundary conditions (fixed lateral, free vertical) and we assume a no-slip boundary condition at the base of the ocean. Post-impact topography at the ice shell/ocean interface is smoothed using a 50-km moving average to avoid sharp boundaries and any associated instabilities they may cause in the FEM.

The FE modeling approach follows the process developed by Freed et al. (2014), in which the thermal evolution of the basin (cooling) is calculated prior to simulating its viscoelastic relaxation (isostatic adjustment). This approach provides numerical efficiency and stability, but inherently assumes there is no significant lateral displacement (10s of km) within the ice during isostatic adjustment. However, our results indicate that lateral flow (on the order of 100 km) can occur in the warmer, basal portion of the ice. Where present, this introduces localized inaccuracies in the final thermal state that influences our results, but not our conclusions, as discussed below.

The FEM approach occurs in four discrete steps (Fig. S1). An initial heat conduction run using the same boundary conditions and temperature-dependent conductivity as the pre-impact state of the iSALE model establishes a background thermal structure to which the post-impact FEM will cool. To hold temperature constant in the ocean, as in the iSALE simulations, the thermal conductivity of the ocean is defined to be two orders of magnitude larger than the largest thermal conductivity in the ice shell. The second step is to emplace the post-

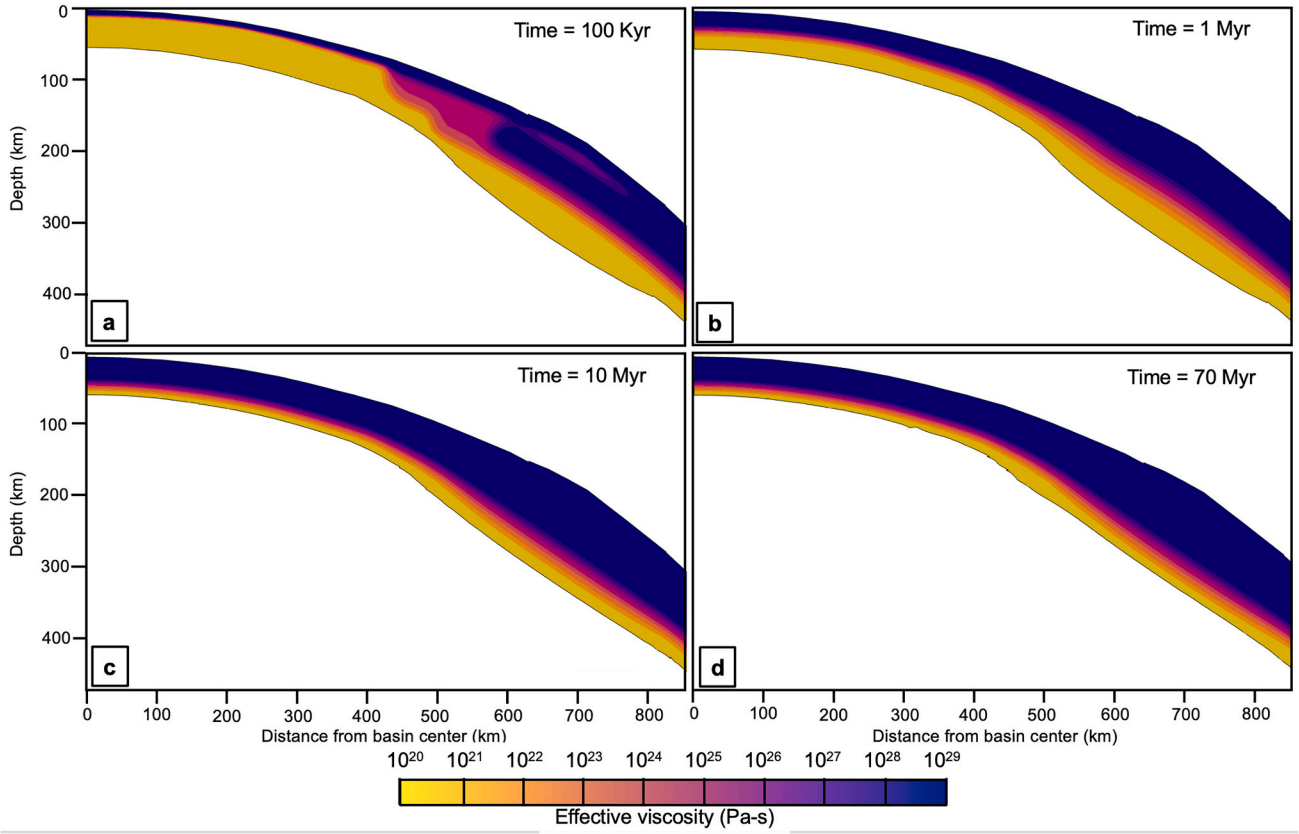

Fig. 6. Time series of the effective viscosity in the ice shell during cooling and isostatic adjustment of Sputnik Planitia for a thin, warm ice shell. For the model shown, the viscosity used is $\eta_b = 10^{15}$ Pa s. Onset of lithosphere formation is deemed to be at $\sim 10^{24}$ Pa s (light purple). For clarity, only the ice shell is shown, as the ocean retains a constant viscosity that is an order of magnitude lower than the lowest ice shell viscosity. (For interpretation of the references to colour in this figure legend, the reader is referred to the web version of this article.)

impact thermal structure from iSALE into the FEM regions thermally perturbed by the impact (Fig. 3), with the remainder of the model retaining the pre-impact background thermal structure. We simplify the thermal structure produced in our iSALE simulations by dividing the FEM into zones of approximately equal temperature. Then a heat conduction calculation is performed until the basin cools to the pre-impact thermal structure. This step establishes the thermal evolution of the basin.

The third step incorporates the final steady-state density structure from the iSALE calculation as the initial density structure of the FEM. The zones of similar temperatures established in the previous steps are used as zones of similar density (with Pluto's low gravity this is a reasonable approximation). For this density structure to revert to the pre-impact density structure after cooling, appropriate coefficients of thermal expansion are assigned to each zone. The required thermal expansion coefficients range from 2 to 5 $\times$ 10^{-5} K^{-1}. In this step, a prestress field is also derived from the calculation of the overburden pressure in each element, that when applied during the viscoelastic stage minimizes self-compression due to gravity. We assume a Poisson's ratio of 0.33, as in iSALE, and a Young's modulus (E) of 1 GPa (Nimmo and Schenk, 2006), a conservative lower bound that facilitates motion in the ice shell during cooling and relaxation.

The fourth and final step calculates the response to viscoelastic flow caused by lateral pressure gradients acting on a temperature-dependent ice rheology as temperatures cool to pre-impact levels. We use a temperature-dependent rheology for the ice shell based on Nimmo (2004), given by:

$$\eta(T) = \eta_b exp\left(\frac{Q(T_b - T)}{RT_bT}\right) \quad (2)$$

where η_b is a reference viscosity taken at an associated reference temperature T_b (270 K), Q is the activation energy (40 kJ mol^{-1}), and R is the universal gas constant (8.314 J K^{-1} mol^{-1}). Reference viscosities of 10^{13} to 10^{17} Pa s have been considered for Pluto's ice shell (Conrad et al., 2019; Kamata and Nimmo, 2014). Thus, we explore a range of reference viscosities between 2.5 $\times$ 10^{14} Pa s, the lowest stable rheology our models can sustain, up to 10^{17} Pa s. When applied to Pluto-like temperatures, this formulation leads to a range of possible ice shell viscosities from extremely weak ($\leq 10^{19}$ Pa s at 200 K) to very strong ($\geq 10^{24}$ Pa s at 140 K) as a function of temperature and reference viscosity (Fig. 4).

Ice viscosities below $\sim 10^{19}$ Pa s will readily flow within a time span of years or less. Such low viscosities can cause numerical instabilities in model runs that simulate millions of years of basin deformation. To avoid such instabilities, we set a minimum viscosity of 5 $\times$ 10^{19} Pa s, as reflected in the vertical solid line in Fig. 4. Numerical experiments confirm that setting such a minimum viscosity does not significantly influence model results, since such viscosities already provide minimal resistance to flow. Similarly, we cannot model water with a near-zero viscosity. However, as shown by Freed et al. (2014), as long as a weak voluminous zone (e.g., a melt pool associated with rocky impacts) is modeled with at least an order of magnitude lower viscosity than neighboring regions whose behavior is expected to be mechanical (e.g., the icy layer), these weak volumes do not significantly influence viscoelastic flow within the mechanical regions. We thus model water with a viscosity of 5 $\times$ 10^{18} Pa s. While some models cannot achieve steady state because of numerical instabilities despite these adjustments, such models invariably run long enough to draw firm conclusions as to where the final state of the basin was heading. We discuss some of these cases in the results section below.

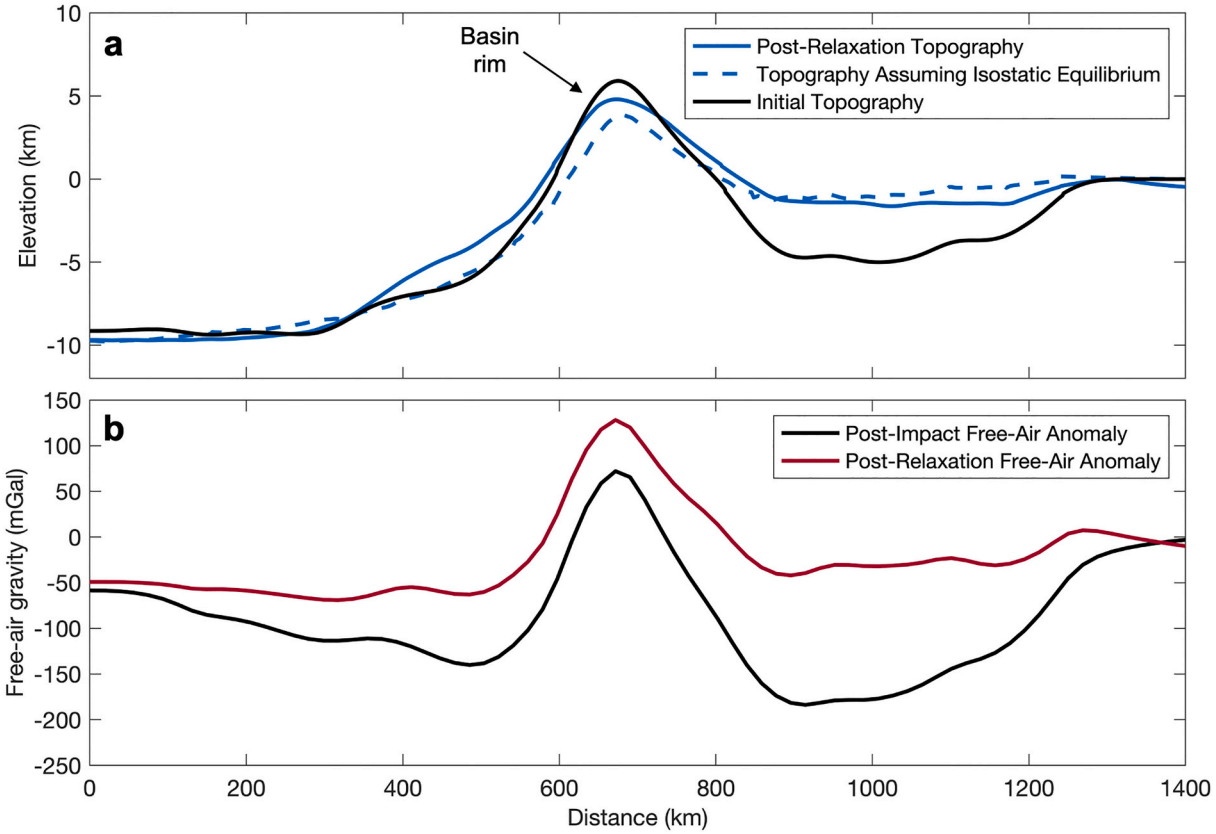

Fig. 7. (a) Basin topography post-impact (black line) and post-cooling and isostatic adjustment (blue line). Shown for reference is the predicted topography assuming isostasy of the post-cooling density structure (dashed blue line) for a thin, warm ice shell with a reference viscosity of $\eta_b = 10^{15}$ Pa s. (b) Calculated free-air gravity anomaly post-impact (black line) and post-cooling and adjustment (red line). (For interpretation of the references to colour in this figure legend, the reader is referred to the web version of this article.)

Once the viscoelastic model reaches steady state, defined by no further significant deformation occurring, we determine the predicted empty basin topography and compute the free-air gravity anomaly following the approach documented in Trowbridge et al. (2020). We use the same code to perform gravitational calculations over a basin as used in Melosh et al. (2013), Freed et al. (2014), and Trowbridge et al. (2020), which is based on the formulation for gravitational acceleration over a ring (Turtle and Melosh, 1997) to calculate the gravity field for the steady-state basin produced in the FEM. We build an additional FEM representing the geoid using an undeformed mesh, i.e., pre-impact conditions. Gravity anomalies are calculated based on taking the difference in the calculated absolute gravities of these two models, computed at an altitude of 30 km above the datum.

One limitation in our modeling is that the evolution of cooling and viscoelastic flow are assumed to be independent processes. This can introduce localized numerical artifacts in our results. If there is significant lateral flow within the ice during isostatic adjustment, the temperature within that region will not reflect this deformation. This only occurs within the weakest rheologies and only along the base of the ice where material is weakest. Inaccuracies in the evolution of temperature in these regions lead to inaccuracies in the evolution of density, surface topography, and the calculated gravity anomaly. Such inaccuracies are easily identified and do not influence the conclusions drawn from these runs, which are typically poor fits to the basin due to the predominance of weak material in the ice shell.

4. Results

We seek to find the set of conditions (initial ice shell thickness, thermal structure, and temperature-dependent rheology) that lead to a final basin configuration consistent with that inferred for the SP basin prior to N_2 fill (~1300 km in diameter, 3–10 km deep relative to Pluto's surface, with an ~1 km-high rim) and determine whether such configurations are isostatically compensated. Results for all four scenarios tested are summarized in Table 4.

4.1. Thin, warm: 100-km ice shell, $T_b = 192$ K

Our thin, warm ice shell scenario, which incorporates a 332-km-diameter impactor, a 100-km-thick ice shell, and an ice shell basal temperature of 192 K, produces multiple plausible basin interiors over a range of ice rheologies consistent with the observational constraints. Basin formation begins with the excavation of the transient crater, as the large, slow-moving impactor spreads into a thin layer of cold material lining the interior of the deep, bowl-shaped transient crater, which is ~275 km deep at its deepest point in time (Fig. 5a). The transient crater then succumbs to gravity-driven collapse, producing a large central uplift reaching ~800 km above the surface (Fig. 5b). Collapse of the uplift pushes ice outwards over the rim of the transient crater. Ice dislodged within the ocean then floats upward to rejoin the overlying shell, after which modification is complete (Fig. 5c).

Final basin morphology following transient crater collapse for a thin, warm ice shell includes thinned ice in the inner ~400 km of the basin interior, thickened ice in an ~300 km zone in and around the basin rim, similar to a crustal collar, and a slightly depressed region that lies outside the rim (Fig. 5c). At the surface, the basin possesses a broad, 9-km deep interior surrounded by a 200-km-wide topographic high produced from accumulation of ejecta and material splashed out during collapse of the central uplift. Material that is splashed out is deposited on top of the preexisting crater rim, creating a broader, taller rim than

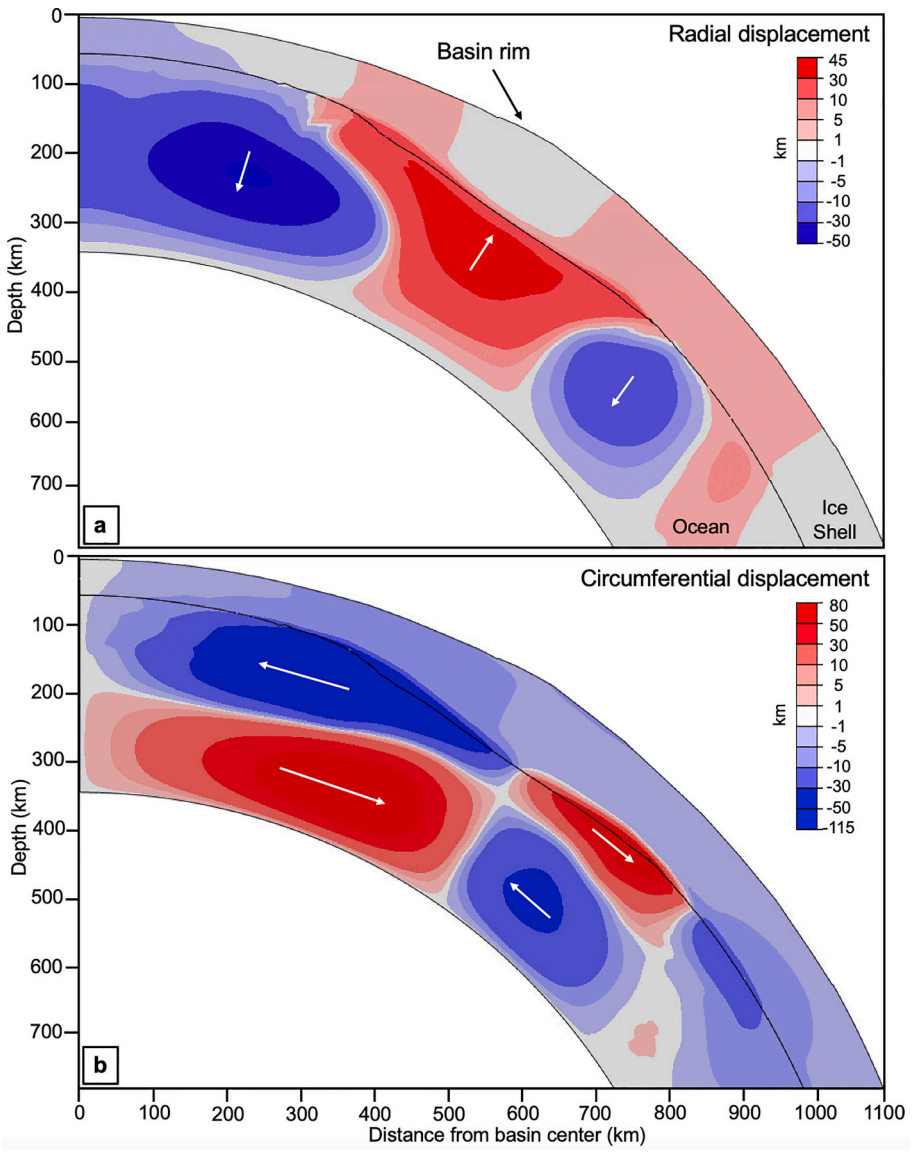

Fig. 8. FEM calculations of (a) radial and (b) circumferential displacements due to cooling and isostatic adjustment of Sputnik Planitia following transient crater collapse for a thin, warm ice shell. The model shown uses $\eta_b = 10^{15}$ Pa s, the average predicted rheology for Pluto's ice shell as its reference viscosity. Black curves denote material interfaces (top of ice shell, ice shell-ocean interface, base of ocean). For radial displacement, positive (red) displacement indicates upward motion and negative (blue) is downward. For circumferential displacement, positive (red) values indicate outward motion with respect to the symmetry axis, while negative displacement (blue) is inward. (For interpretation of the references to colour in this figure legend, the reader is referred to the web version of this article.)

otherwise expected, as well as artificially increasing basin depth (Silber and Johnson, 2017). Thinned ice in the basin interior is interrupted by an accumulation of ice near the symmetry axis ~ 50–100-km from the basin center, a feature which is more pronounced when the ice shell is thicker. As noted by Johnson et al. (2016), this feature is a consequence of an axially symmetric model, which exaggerates central uplift heights (also enhancing the amount of material splashed out). We remove this feature when importing topography into the FEM (see Section 3.2), as it is assumed to be an artifact of axisymmetry.

In the FEM, the impact-induced thermal anomaly takes ~70 Myr to cool and return to its pre-impact thermal structure. However, most of the ice shell returns to its pre-impact thermal structure within only ~10 Myr, after which cooling slows markedly and is limited to the thickened portion of the ice shell. Fig. 6 shows how this cooling leads to the development of a lithosphere as a function of time. For our purposes, we define the lithosphere as the region within which the viscosity $\geq 10^{24}$ Pa s, as such regions do not relax differential stresses significantly on timescales of 10s of millions of years. A lithosphere of only ~10 km thick following transient crater collapse (Fig. 6a) grows to ~60-km-thick after 10 million years of cooling (Fig. 6c).

The change in topography and free-air gravity anomaly from post-impact (initial FEM) through post-cooling and isostatic adjustment is shown in Fig. 7. Fig. 7a also shows the topography required to be in isostatic equilibrium associated with the initial density structure. In this framework, we use an inferred average pre-impact ice shell and ocean density and assume that, without N_2 loading, the mass anomaly associated with the oceanic uplift must balance the mass deficit associated with the surface topography, such that the pre-impact ice shell thickness can be used to calculate expected topography for an isostatically compensated basin. This serves as a reference to determine whether the initial FEM topography is isostatically compensated. Fig. 7 reveals that following impact, inner basin topography is near isostatic equilibrium (initial model topography is equal to isostatic equilibrium topography), the basin rim is superisostatic (initial model topography is higher than isostatic equilibrium topography), and the outer basin is subisostatic (initial model topography is lower than isostatic equilibrium topography).

While isostatic equilibrium is commonly associated with a zero free-air anomaly, this is not exactly the case. The depth of the compensating material (in this case the ocean), which is ~60 km below the pre-impact surface, decreases its contribution to the measured gravity field, such that a small negative anomaly remains. Thus, we consider the free-air anomaly shown in Fig. 7b to be consistent with the inner basin's isostatic state following cooling.

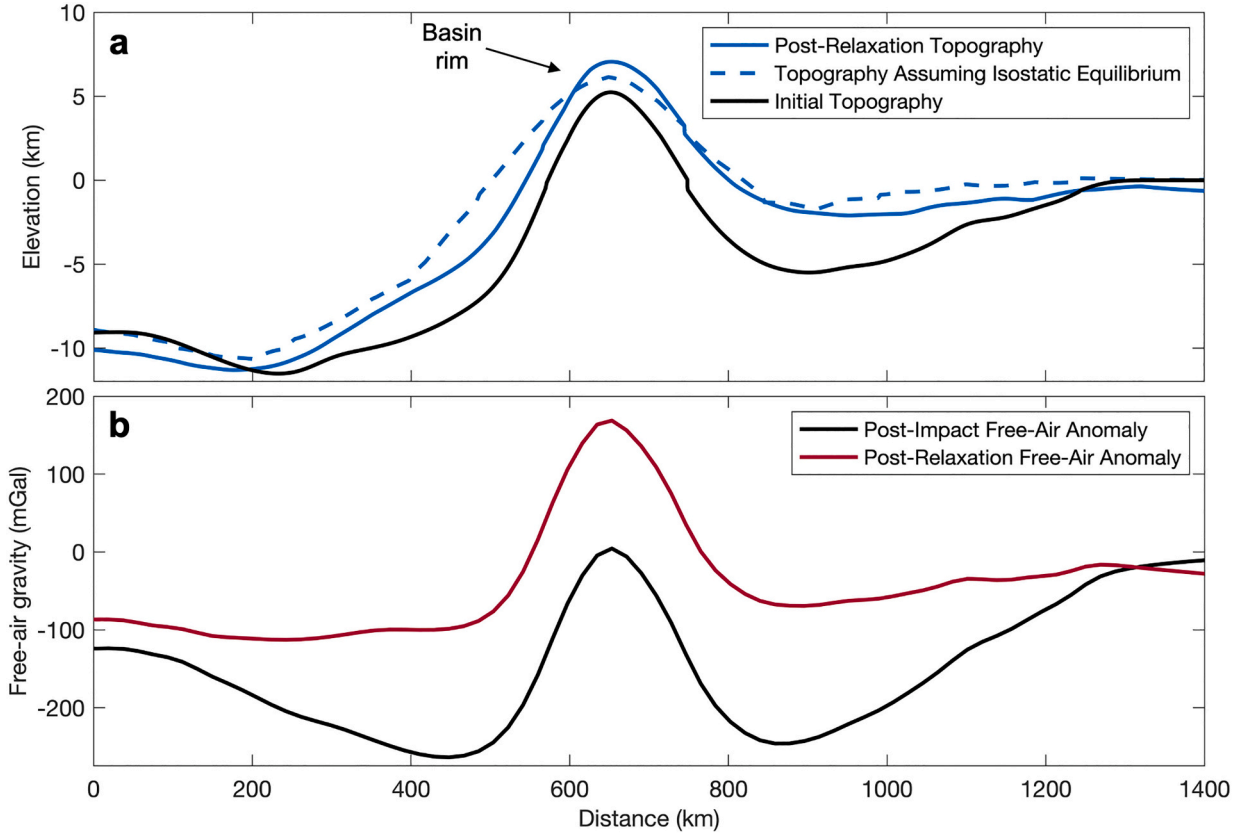

Fig. 9. (a) Topography for the post-impact (black line) and post-cooling and adjustment (blue line) basin in comparison to the predicted topography assuming isostasy (dashed blue line) for a reference viscosity of $\eta_b = 10^{15}$ Pa s used to reproduce SP for a thin, cold ice shell. (b) Calculated free-air gravity anomaly post-impact (black line) and post-cooling and adjustment (red line). (For interpretation of the references to colour in this figure legend, the reader is referred to the web version of this article.)

While this basin matches SP's current estimated depth and diameter, the final basin rim is significantly higher than observed (~4.7 km vs. ~1 km, Schenk et al., 2018). The taller rim may result from material splashed out during basin formation, a feature driven of axisymmetric model design, as well as insufficient subsidence during cooling and isostatic adjustment (discussed below). Morphological analysis of SP's rim terrain also suggests significant post-impact modification has occurred in the ensuing ~3 Gyr since its formation (Schenk et al., 2018; McGovern et al., 2021).

Complementary to Fig. 7, Fig. 8 shows the total radial and circumferential displacement that occurs due to cooling and isostatic adjustment throughout the ice shell. The inner basin is shown to subside, while regions outside the basin rise. At the surface, the inner basin only subsides about 1 km, while larger subsidence (10s of km) occurs in the subsurface (Fig. 8a). Subsidence of the inner basin is caused by contraction associated with cooling. Since the inner basin is initially close to isostatic equilibrium, the major source of displacement is cooling. This small amount of surface subsidence at the basin center is consistent throughout all tested rheologies, leading to a final basin depth of ~10 km, consistent with the deeper end of the inferred depth of SP prior to ice fill.

Outside the basin (beyond 850 km from the basin center), the initial temperatures are not significantly different from background temperatures (Fig. 6a), and there is no significant contraction due to cooling. However, this region is strongly undercompensated isostatically (due to an annulus of low topography outside the rim) such that isostatic forces are significant and cause the ice shell to rise ~3 km until equilibrium is achieved (Fig. 8a). Topography in the region around the basin rim (650 km from the basin center) is initially superisostatic due to rim topography and subsides due to isostatic forces. However, the rim does not subside sufficiently to achieve isostatic equilibrium because this region is mechanically attached to the thick lithosphere in the region outside the rim, which is rising due to isostatic forces. The volume of the annulus of low topography outside the rim is much larger than the annulus of high rim topography. Thus, isostatic forces outside the rim are sufficient to bring the region close to isostatic equilibrium while preventing the rim from doing so. This result is not substantially changed for all rheologies tested.

Corresponding circumferential displacement illustrates that modest lateral flow occurs in the ice shell in the inner basin, with greater inward flow occurring within the upper half of the subsurface ocean (Fig. 8b). This inward motion is caused by contraction associated with cooling of the inner basin. Surface uplift on either side of the basin rim requires uplift of the subsurface ocean beneath the region (Fig. 8a). This in turn requires water to be drawn into the area, which occurs from the lower half of the subsurface ocean (note arrows in Fig. 8b). Thus, water in the lower half of the ocean moves laterally outwards from the inner basin and laterally inwards from the outer basin beneath the extended rim region.

4.2. *Thin, cold: 100-km ice shell, $T_b = 120$ K*

We find that our thin, cold ice shell scenario, which incorporates the same initial conditions as the thin, warm scenario but with a lower basal temperature of 120 K, also produces a basin consistent with the inferred characteristics of SP prior to N_2 ice loading for a wide range of assumed rheologies. The resulting basin is morphologically similar to the thin, warm ice shell following impact. Morphologic similarities between thermal structures are likely due to the influence of the ocean as a large strengthless layer beneath the thin ice shell. This suggests that the

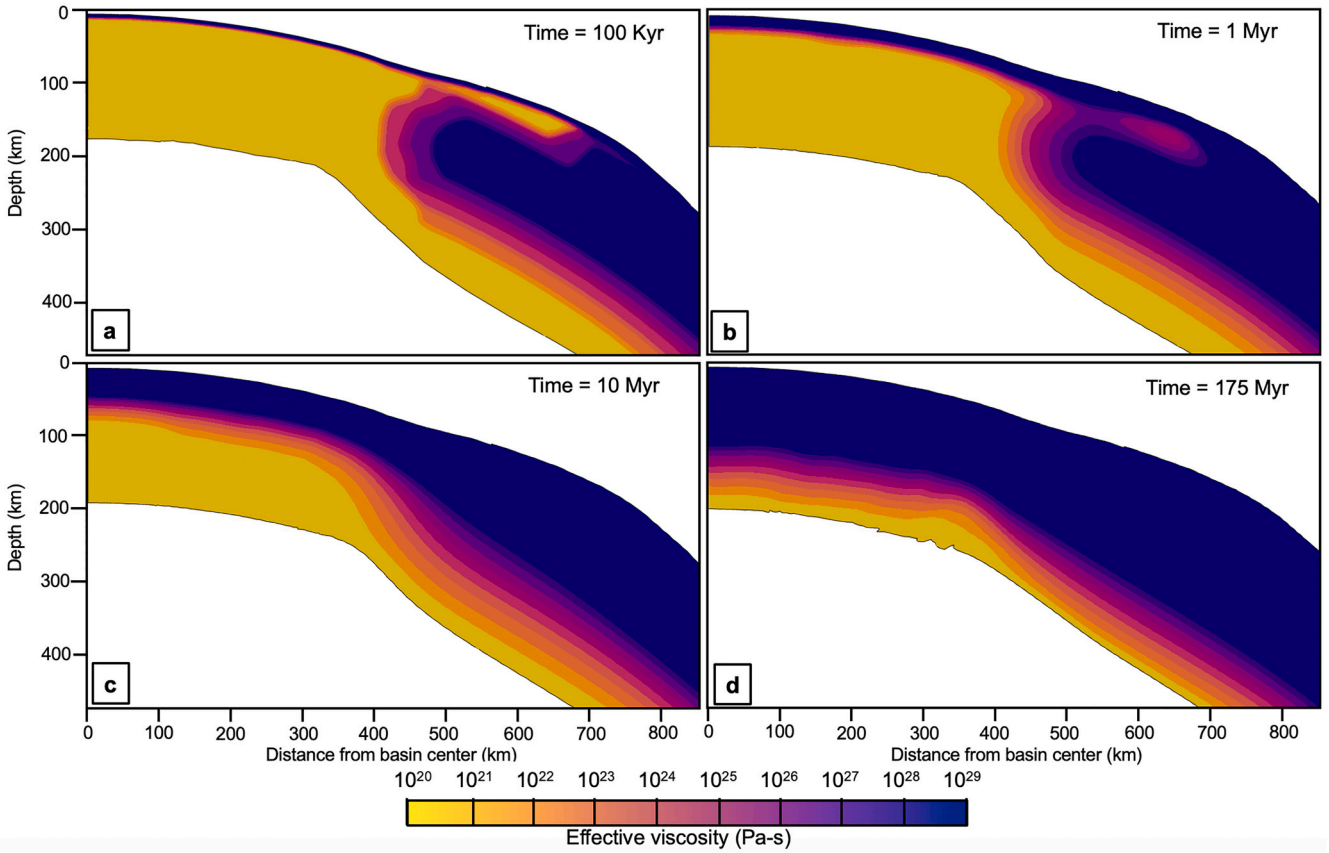

Fig. 10. Time series of the effective viscosity in the ice shell during cooling and isostatic adjustment of Sputnik Planitia for a thick, warm ice shell. For the model shown, the viscosity used is $\eta_b = 7 \times 10^{15}$ Pa s. Onset of lithosphere formation is deemed to be at $\sim 10^{24}$ Pa s (light purple). For clarity, only the ice shell is shown, as the ocean retains a constant viscosity that is an order of magnitude lower than the lowest ice shell viscosity. (For interpretation of the references to colour in this figure legend, the reader is referred to the web version of this article.)

strength contrast between the ice shell and underlying ocean overwhelms the influence of any thermally-derived changes in ice strength during transient crater collapse.

Cooling occurs rapidly and is completed within ~40 Myr. Temperature drops quickly with distance, causing all material at and beyond the basin rim to remain <120 K post-impact and thus to behave elastically during cooling. The basin produced in the cooler scenario begins more isostatically undercompensated prior to cooling and relaxation (Fig. 9) compared to the warmer scenario, most notably to either side of the basin rim, leading to more isostatic uplift in these regions as the basin cools. Due to mechanical coupling of the strong ice outside the basin, the rim, which begins close to isostasy prior to cooling, is actually lifted into a slightly superisostatic position by the time the basin reaches its steady-state configuration prior to N_2-ice loading, leaving the final rim higher than estimated by Schenk et al. (2018) (~7 km). The overall basin (except for the rim) ends up in a slightly negative, subisostatic configuration with similar depth (~10 km) to the thin, warm ice shell scenario (Fig. 9).

4.3. Thick, warm: 200-km ice shell, $T_b = 180$ K

We find that our thick, warm ice shell scenario, which uses a thicker 200-km-thick ice shell and a basal temperature of 180 K, can produce basins consistent with SP prior to loading if the ice shell's viscosity structure is in the stronger portion of the range considered. This scenario requires a slightly larger 340-km-diameter impactor to reproduce the inferred 1300-km average basin diameter. The larger volume of ice mobilized during formation and collapse of the central uplift deposits more material onto and outside of the rim of the transient crater and induces a second, smaller central uplift during transient crater collapse, leading to a longer duration before the basin reaches steady-state. The resulting basin is several km deeper (~12.5 km) compared to the thinner ice shell cases and also possesses a higher rim (~14.4 km). However, the basin exhibits a similar structure, with thinned ice in the interior bordered by an annulus of thickened ice.

The larger volume of impact-heated ice following impact extends the basin's cooling time to ~175 Myr. While cooling occurs rapidly at the surface, temperatures in the inner ~300–400 km of the basin remain elevated in the basal portion of the ice shell until cooling is completed, which prolongs lithosphere development and extends the residence time of weak ice (Fig. 10). The presence of a larger, more long-lived volume of weak ice underlying the lithosphere, which grows to ~145–165 km thick after 175 million years, induces much more widespread deformation in the ice shell.

The corresponding change in topography and free-air gravity for this scenario is shown in Fig. 11. The post-collapse basin for the thick, warm ice shell is strongly subisostatic (Fig. 11) compared to the thinner ice shells explored. As a result, isostatic forces cause the inner basin to rise during cooling, in this case ~5.5 km, to evolve towards isostatic equilibrium (Fig. 11a). This is in contrast to the thin ice shell cases, where the inner basin subsides due to contraction associated with cooling in the absence of significant isostatic forces. Similar to the thin ice shells tested, the initially superisostatic rim subsides due to isostatic forces, but not sufficiently to achieve isostatic equilibrium, as it is held up by being mechanically connected through a strong lithosphere to the rising regions that surround it (Fig. 10). This also keeps the rim significantly higher than observed (~11 km).

Fig. 12 shows cumulative displacement throughout the ice shell and

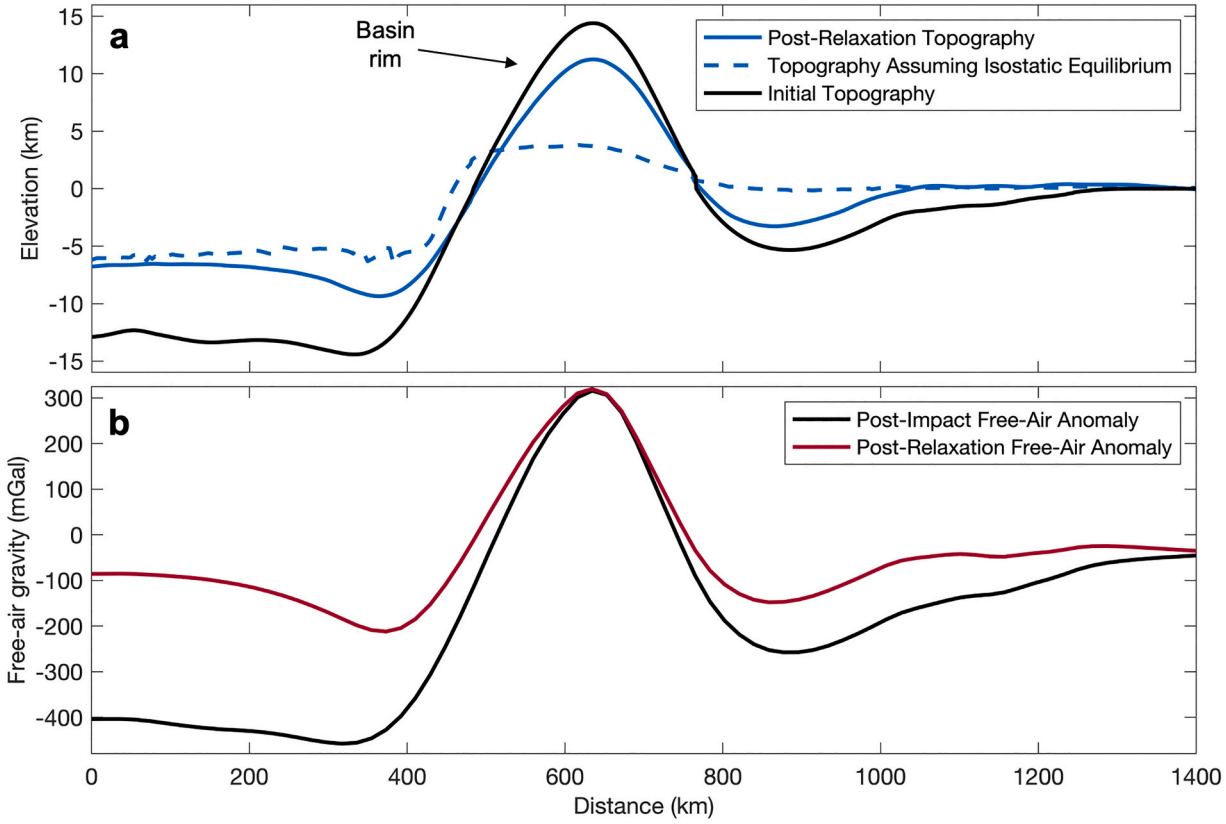

Fig. 11. (a) Topography for the post-impact (black line) and post-cooling and adjustment (blue line) basin in comparison to the predicted topography assuming isostasy (dashed blue line) for one of the thick, hot ice shell models which best reproduces SP ($\eta_b = 7 \times 10^{15}$ Pa s). (b) Calculated free-air gravity anomaly post-impact (black line) and post-cooling and adjustment (red line). (For interpretation of the references to colour in this figure legend, the reader is referred to the web version of this article.)

underlying subsurface ocean for $\eta_b = 7 \times 10^{15}$ Pa s. In general, the sense of vertical displacement at the surface extends downwards throughout the ice shell (Fig. 12a). As with the thinner cases, inward circumferential flow is primarily concentrated in the ocean (Fig. 12b). Inward flow in the upper half of the ocean beneath the basin center is required to support the uplift of this region in the ice shell. This flow direction also enables subsidence of the basin rim, as does outward flow in the upper ocean outside the rim. As with the thinner cases, flow directions are reversed in the lower half of the subsurface ocean.

When the ice shell is rheologically weak (e.g., $\eta_b = 2.5 \times 10^{14}$ Pa s), viscoelastic flow is sufficient to relax the surface of the basin to zero topography, such that the basin interior effectively returns to a pre-impact ice shell. Thus, models with weaker rheologies do not lead to basin topography consistent with that inferred prior to N_2 ice filling.

4.4. Thick, cold: 200-km ice shell, $T_b = 120$ K

Our thick, cold ice shell scenario, which uses the same initial conditions as the thick, warm ice shell but with a basal temperature of 120 K, does not produce an SP-like basin, regardless of the ice rheology assumed. The initial basin is ~18-km deep following impact, much deeper than the other cases, with a comparably large rim (~15.8 km). Faster cooling (~150 Myr) compared to the hot, thick scenario facilitates rapid lithosphere formation. Combined with the cold, strong ice surrounding the basin, this limits the isostatic response even for the weakest rheology tested ($\eta_b = 2.5 \times 10^{14}$ Pa s; Fig. 13). While a small amount of uplift (~3 km) reduces the free-air anomaly somewhat, the final basin remains on the order of ~15-km deep with a 15-km-high rim (Fig. 13a) and a strongly negative free-air gravity anomaly while unloaded (Fig. 13b). Thus, cooling and limited isostatic adjustment largely preserve the post-impact topography, such that the initial conditions associated with a thick, cold ice shell do not lead to a basin consistent with the characteristics observed for SP.

5. Discussion

5.1. Implications for mascon basin formation

Previous analysis of SP by Johnson et al. (2016) favored mascon formation in a loaded basin for ice shells ≤178 km. However, our calculations suggest that the thermal conditions assumed in that study would enable substantial post-impact relaxation, likely removing the uplifted ocean and producing an excessively shallow basin. However, our results suggest that a mascon basin following N_2 loading, as predicted by Nimmo et al. (2016), may be viable if the ice shell is thin. Our 100-km-thick ice shell scenarios preserve the uplifted ocean, which is critical to maintaining a low free-air anomaly in the empty basin; the volume of N_2 ice that is otherwise required to produce a mascon basin in an uncompensated SP exceeds current thickness estimates by an order of magnitude (Nimmo et al., 2016; Nimmo and McKinnon, 2021). However, we must further consider whether a good fit to an empty SP is also consistent with SP once loaded with N_2. Our FEMs do not account for the subsequent loading of the basin with N_2 ice; however, analytical estimates can approximate the effects of loading and subsidence. We note that other authors have investigated the role of N_2 ice loading in relation to Pluto's possible reorientation (Hamilton et al., 2016; Keane et al., 2016; Nimmo et al., 2016; Mills and Montesi, 2019; Johnson et al., 2021).

We use the axially-symmetric spherical flexure equation (e.g., Brotchie and Silvester, 1969; Comer et al., 1985) to calculate the effects

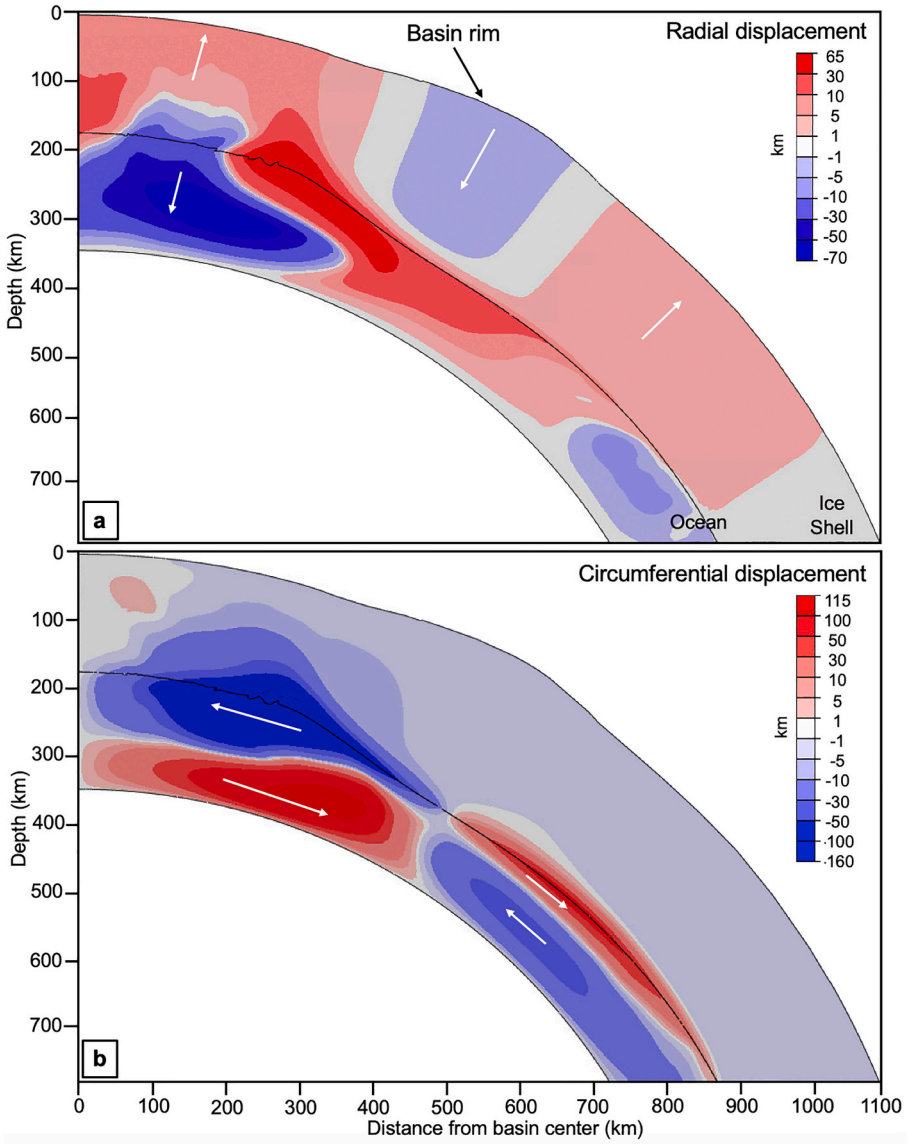

Fig. 12. FEM calculations of (a) radial and (b) circumferential displacements due to cooling and isostatic adjustment of Sputnik Planitia following transient crater collapse for a thick, warm ice shell. The model depicted uses $\eta_b = 7 \times 10^{15}$ Pa s as its reference viscosity.

of a parabolically-shaped load of N_2. We consider a range of 3–10-km-thick N_2 ice at the basin center that tapers to zero at the edge of the basin (defined to be the average basin radius, 650 km). We assume elastic lithosphere thicknesses derived from the FEM, using the average depth at which the ice shell behaves elastically during our simulations ($\eta \geq 10^{24}$ Pa s). Using topographic profiles from the post-cooling basin, we generate new topography that incorporates load geometry and ice shell subsidence.

Our analytical loading estimates find that for the deep (~10 km) post-cooling basins formed in a thin ice shell, thinner N_2 loads (3–5 km) are insufficient in shallowing the basin to within current estimates. Increasing the thickness of the ice load (up to 10 km) also cannot sufficiently reduce basin depth, as the larger volume of N_2 ice induces increasing amounts of subsidence that keeps the basin deep. The minimum depth of the loaded basin in this scenario is ~8 km, exceeding current estimates for loaded basin depth (~3 km, Schenk et al., 2018). Thus, while thin ice shells feasibly reproduce an unloaded SP, additional basin modification may be required in conjunction with N_2 loading to sufficiently match observed topography. In particular, a stronger ice shell and/or a shallower initial basin may adequately support the load, allowing the additional mass to drive the basin towards a positive mass anomaly. Other interpretations of Pluto's elastic response have assumed a higher Young's modulus ranging from 5 to 9 GPa (Nimmo et al., 2016; McGovern et al., 2021), which would reduce the amount of subsidence from N_2 loading. A shallower initial basin may also be possible given different initial conditions prior to impact, as well as the likelihood of further modification shallowing the basin interior. Morphological analysis of SP suggests significant post-impact erosion has occurred in the ~3 Gyr since its formation (Schenk et al., 2018).

By contrast, a thick, warm ice shell better supports N_2 loads due to its more substantial lithosphere and shallower basin depths post-cooling, such that loading can produce basins within ~1 km of estimates for variable N_2 thicknesses. However, the final basin configuration for a thick, warm ice shell lacks a subsurface contribution to the free-air gravity anomaly due to removal of the uplifted ice shell-ocean interface. Thus, a thick, warm ice shell can feasibly produce an SP-like basin up to and including loading by N_2 ice, but the resulting structure is not likely to become a mascon basin.

At present, our simulations approach the current expected unloaded geometry and underlying structure of SP. While our analytical loading estimates suggest that producing a mascon basin in SP is unlikely under our current model suite, as noted above, several additional variables

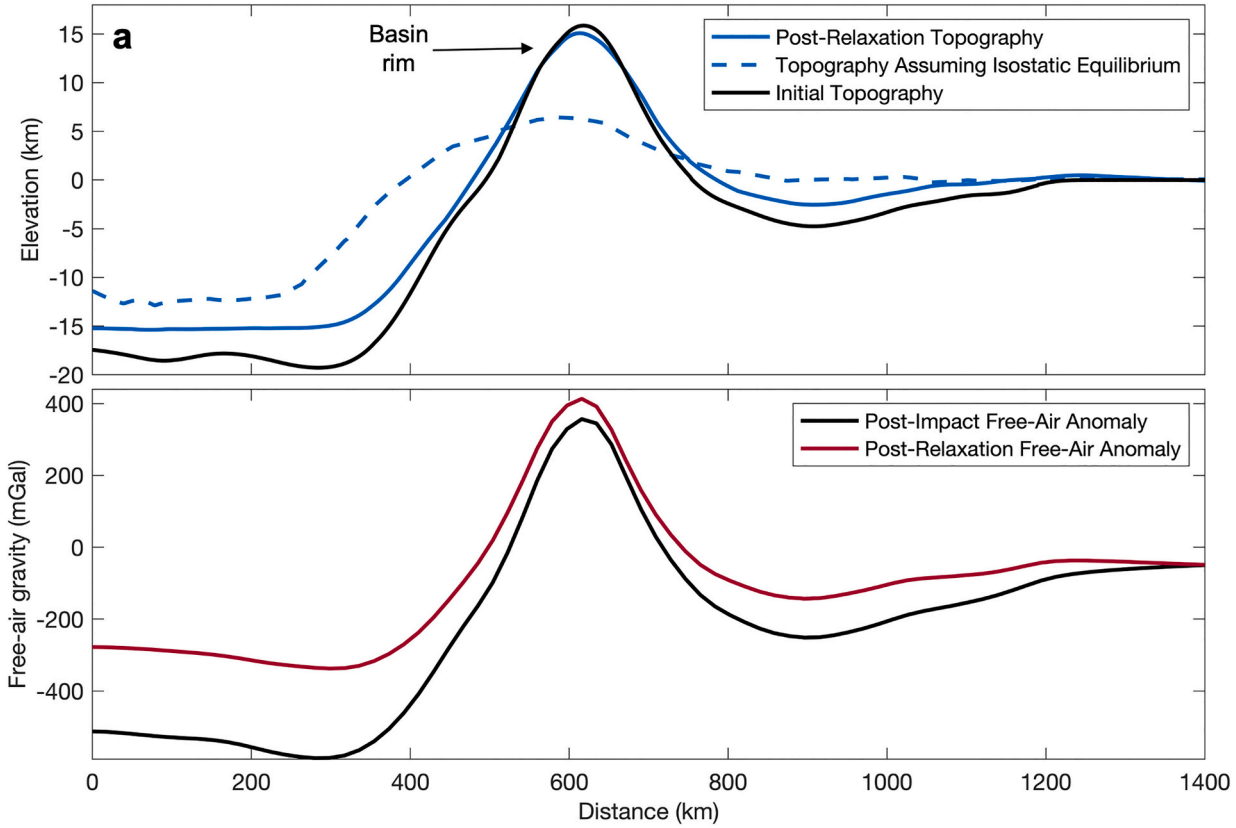

Fig. 13. (a) Topography of SP for the weakest viable test case for a thick, cold ice shell post-impact (black line) and post-cooling and adjustment (blue line) in comparison to the predicted topography assuming isostasy (dashed blue line). (b) Calculated free-air gravity anomaly post-impact (black line) and post-cooling and adjustment (red line). (For interpretation of the references to colour in this figure legend, the reader is referred to the web version of this article.)

may facilitate the formation of a mascon basin and should be explored in future work. These include: the possibility of a stiffer ice shell (e.g., higher Young's modulus), a shallower initial basin, which may be produced through further in-depth exploration of thin ice shells and their variable thermal structures, as well as an investigation of the role of post-impact erosion on basin rim and floor morphology.

5.2. Implications for alternative ice shell structures

The extensive computation time required for this work limits the number of scenarios for Pluto's interior that we can consider. As such, we focused on the most plausible conditions for Pluto's ice shell: that it is either thin (on the order of ~100 km) or thick (on the order of ~200 km), and that the ice shell, assumed to be conductive, either remains warm enough to sustain a liquid ocean (Nimmo et al., 2016), or is much colder due to insulation by methane clathrates (Kamata et al., 2019).

The ice shell is unlikely to be colder than tested here, as 120 K presents the lower limit of ice shell basal temperatures that can be permitted with a methane clathrate layer while still enabling the presence of a liquid ocean. However, if the SP-forming impact occurred into a colder ice shell, the resulting basin would likely be even deeper than those observed in our cold cases and respond minimally to subsequent cooling and isostatic adjustment. Thus, a match to SP is unlikely if the ice shell is cooler than tested here. A warmer ice shell is also unlikely to reproduce SP, as a thick lithosphere is necessary to preserve basin topography and a warmer shell would thin the lithosphere, reducing its capacity to preserve topography in and around SP. An ice shell with a larger volume of warm, deforming ice than explored in our models will flow readily, and, if the ice shell is sufficiently weak, remove topography in the basin entirely. This trend will be further enhanced if the lower portion of the ice shell is convecting, which is likely to occur when the ice shell is warm.

Reproducing SP is also unlikely if the ice shell is much thinner than our 100-km scenario. If the ice shell is sufficiently thin, the impactor may completely penetrate the ice shell, exposing the ocean directly to space (e.g., Roberts and Stickle, 2021) or otherwise entraining large volumes of water in the ice shell during collapse. While it is difficult to determine how a basin with a portion of exposed or near-surface ocean may evolve, an exposed ocean will likely delay formation of the lithosphere due to the prolonged cooling times, and the final basin structure, including depth and interior ice shell thickness, is unknown. If a basin persists and approaches isostatic equilibrium following cooling, as in our 100-km cases, a thinner ice shell would also experience greater subsidence, further limiting its ability to maintain a reasonable depth following N_2 loading. A sufficient match to SP is also unlikely if the ice shell is much thicker than the 200-km-thick ice shell explored here. If the ice shell is even thicker, the prevalence of cold, strong ice will likely lead to much more lithospheric support, producing a basin much deeper than that inferred of SP prior to ice loading.

While our models successfully reproduce reasonable unloaded basin depths for SP, the basin rim in all simulations is significantly higher than observed by at least several km (Schenk et al., 2018). As noted in Section 4.1, our overestimated rim heights may result from the conditions of axisymmetry, though they may also reflect the limits of our current understanding of ice strength, as material models and equations of state appropriate for ice under outer Solar System conditions are still an area of active research and development. Morphological analysis of SP's rim terrain also suggests significant post-impact modification of the rim has occurred in the ~3 Gyr since its formation, including the formation of numerous impact craters, scouring by copious gullies inferred to be glacial in origin, and ongoing incision by active glacial activity (Schenk et al., 2018). Additionally, we have not explored the effect of a clathrate

layer at the base of the ice shell. Since the clathrate layer is suggested to be much thinner (~3–10-km-thick) than the overlying ice shell (Kamata et al., 2019), it is not expected to influence the large-scale deformation characteristic of basin formation. However, its presence could influence subsequent evolution by limiting flow at the ice shell base during cooling and relaxation and should be explored in future FEM work.

6. Conclusions

We have applied a combination of a shock physics code and finite element modeling to simulate the formation of Sputnik Planitia from impact through cooling and isostatic adjustment, prior to loading by N_2 ice. We explored the effects of ice shell/ocean thickness, pre-impact thermal structure, and ice shell rheology on the morphology of the resulting basin. Our models successfully reproduce SP's current average diameter of ~1300 km and inferred below-ice depth for a range of thermal and viscosity structures for Pluto's ice shell. Our simulations indicate that basin evolution is significantly influenced by the assumed ice shell thickness and thermal structure. Results suggest that a thin, approximately 100-km ice shell overlying a thick 228-km ocean can reproduce SP for both warm ($T_b = 192$ K) and cold ($T_b = 120$ K) thermal structures, while a thick, 200-km ice shell can reproduce SP if the ice shell is relatively warm yet possesses a strong rheology. An ice shell that is significantly thinner or thicker than tested here, or that exceeds the minimum and maximum basal temperatures tested, is unlikely to reproduce SP, as the final basin will likely either be overly deep or relax away most of its topography. We find that the SP basin was likely close to isostatic equilibrium and not a mascon basin prior to ice fill. Following N_2 ice fill, SP could have developed into a mascon basin if the basin begins isostatic and the ice shell possesses an extensive lithosphere, which could be consistent with a basin formed from an impact into a thin ice shell that is cold enough to be primarily conductive. In the future, it may be interesting to look at coupling the models presented here with N_2-ice infilling models (e.g., Johnson et al., 2021) to build a more complete time history of the SP basin.

The models tested here sample a portion of proposed conditions for Pluto's ice shell to contrast alternative interpretations of Pluto's interior and provide a benchmark on SP's post-impact behavior. However, many of the details regarding both the current state and evolution of SP will remain uncertain without new, in situ geophysical measurements. The proposed Persephone mission concept to orbit Pluto (Howett et al., 2021) could be one avenue for acquiring these measurements, including global gravity and topography data. In the absence of a return to Pluto, continued study of other large impact basins on icy worlds – including the moons of Jupiter, Saturn, Uranus, and Neptune, along with other Kuiper Belt Objects – may provide indirect insight into SP.

Supplementary data to this article can be found online at https://doi.org/10.1016/j.icarus.2023.115541.

Declaration of Competing Interest

None.

Data availability

Data will be made available on request.

Acknowledgments

We gratefully acknowledge the developers of iSALE, including Gareth Collins, Kai Wünnemann, Dirk Elbeshausen, Tom Davison, and Boris Ivanov. Some plots in this study were created with the pySALEPlot tool written by Tom Davison. This work was supported by NASA's FINESST program (80NSSC20K1370).

References

Amsden, A.A., Ruppel, H.M., Hirt, C.W., 1980. SALE: A Simplified ALE Computer Program for Fluid Flow at all Speeds. Los Alamos, NM (United States). https://doi.org/10.2172/5176006.

Benz, W., Cameron, A.G.W., Melosh, H.J., 1989. The origin of the moon and the single-impact hypothesis III. Icarus 81 (1), 113–131. https://doi.org/10.1016/0019-1035(89)90129-2.

Bierson, C.J., Nimmo, F., Stern, S.A., 2020. Evidence for a hot start and early ocean formation on Pluto. Nat. Geosci. 13 (7), 1–5. https://doi.org/10.1038/s41561-020-0595-0.

Bray, V.J., Collins, G.S., Morgan, J.V., Melosh, H.J., Schenk, P.M., 2014. Hydrocode simulation of Ganymede and Europa cratering trends - how thick is Europa's crust? Icarus 231, 394–406. https://doi.org/10.1016/j.icarus.2013.12.009.

Brotchie, J.F., Silvester, R., 1969. On crustal flexure. J. Geophys. Res. 74 (22), 5240–5252. https://doi.org/10.1029/JB074I022P05240.

Citron, R., Manga, M., Hemingway, D., 2018. Timing of oceans on Mars from shoreline deformation. Nature 555, 643–646. https://doi.org/10.1038/nature26144.

Collins, Gareth S., Jay Melosh, H., Ivanov, B.A., 2004. Modeling damage and deformation in impact simulations. Meteorit. Planet. Sci. 39 (2), 217–231. https://doi.org/10.1111/j.1945-5100.2004.tb00337.x.

Comer, R.P., Solomon, S.C., Head, J.W., 1985. Mars: thickness of the lithosphere from the tectonic response to volcanic loads. Rev. Geophys. 23 (1), 61–92. https://doi.org/10.1029/RG023I001P00061.

Conrad, J.W., Nimmo, F., Schenk, P.M., McKinnon, W.B., Moore, J.M., Beddingfield, C. B., et al., 2019. An upper bound on Pluto's heat flux from a lack of flexural response of its normal faults. Icarus 328, 210–217. https://doi.org/10.1016/j.icarus.2019.03.028.

Davison, T.M., Collins, G.S., Ciesla, F.J., 2010. Numerical modelling of heating in porous planetesimal collisions. Icarus 208 (1), 468–481. https://doi.org/10.1016/j.icarus.2010.01.034.

Denton, C.A., Johnson, B.C., Wakita, S., Freed, A.M., Melosh, H.J., Stern, S.A., 2021. Pluto's antipodal terrains imply a thick Subsurface Ocean and hydrated Core. Geophys. Res. Lett. 48 (2) https://doi.org/10.1029/2020GL091596 e2020GL091596.

Elbeshausen, D., Melosh, J., 2020. A nonlinear and time-dependent visco-elasto-plastic rheology model for studying shock-physics phenomena. Eng. Rep. https://doi.org/10.1002/eng2.12322 e12322.

Freed, A.M., Johnson, B.C., Blair, D.M., Melosh, H.J., Neumann, G.A., Phillips, R.J., et al., 2014. The formation of lunar mascon basins from impact to contemporary form. J. Geophys. Res. E: Planets. https://doi.org/10.1002/2014JE004657.

Hamilton, D.P., Stern, S.A., Moore, J.M., Young, L.A., 2016. The rapid formation of sputnik Planitia early in Pluto's history. Nature 540 (7631), 97–99.

Howett, C.J., Robbins, S.J., Holler, B.J., Hendrix, A., Fielhauer, K.B., Perry, M.E., et al., 2021. Persephone: a Pluto-system orbiter and Kuiper Belt explorer. Planet. Sci. J. 2 (2) https://doi.org/10.3847/PSJ/abe6aa.

Ivanov, B., Melosh, H., Pierazzo, E., 2010. Basin-forming impacts: reconnaissance modeling. Am. Spec. Paper 465, 29–49. https://doi.org/10.1130/2010.2465(03).

Johnson, B.C., Bowling, T.J., Trowbridge, A.J., Freed, A.M., 2016. Formation of the sputnik Planum basin and the thickness of Pluto's subsurface ocean. Geophys. Res. Lett. https://doi.org/10.1002/2016GL070694.

Johnson, B.C., Sheppard, R.Y., Pascuzzo, A.C., Fisher, E.A., Wiggins, S.E., 2017. Porosity and salt content determine if subduction can occur in Europa's ice Shell. J. Geophys. Res.: Planets 122 (12), 2765–2778. https://doi.org/10.1002/2017JE005370.

Johnson, P.E., Keane, J.T., Young, L.A., Matsuyama, I., 2021. New constraints on Pluto's Sputnik Planitia ice sheet from a coupled reorientation–climate model. Planet. Sci. J. 2 (5), 194.

Kamata, S., Nimmo, F., 2014. Impact basin relaxation as a probe for the thermal history of Pluto. J. Geophys. Res.: Planets 119 (10), 2272–2289. https://doi.org/10.1002/2014JE004679.

Kamata, S., Nimmo, F., Sekine, Y., Kuramoto, K., Noguchi, N., Kimura, J., Tani, A., 2019. Pluto's ocean is capped and insulated by gas hydrates. Nat. Geosci. 1 https://doi.org/10.1038/s41561-019-0369-8.

Keane, J.T., Matsuyama, I., Kamata, S., Steckloff, J.K., 2016. Reorientation and faulting of Pluto due to volatile loading within sputnik Planitia. Nature 540. https://doi.org/10.1038/nature20120.

McGovern, P.J., White, O.L., Schenk, P.M., 2021. Tectonism and enhanced Cryovolcanic potential around a loaded sputnik Planitia Basin, Pluto. J. Geophys. Res.: Planets 126 (12). https://doi.org/10.1029/2021JE006964 e2021JE006964.

McKinnon, W.B., Nimmo, F., Wong, T., Schenk, P.M., White, O.L., Roberts, J.H., et al., 2016. Convection in a volatile nitrogen-ice-rich layer drives Pluto's geological vigour. Nature 534 (7605), 82–85. https://doi.org/10.1038/nature18289.

Melosh, H.J., Freed, A.M., Johnson, B.C., Blair, D.M., Andrews-Hanna, J.C., Neumann, G. A., et al., 2013. The origin of lunar mascon basins. Science 340 (6140), 1552–1555. https://doi.org/10.1126/science.1235768.

Mills, A.C., Montesi, L.G.J., 2019. Elastic Flexure Around Sputnik Planitia, Pluto, and Evidence for a Very High Heat Flux. Pluto System After New Horizons. LPI Contribution No, 2133, p. 7030.

Moore, J.M., McKinnon, W.B., Spencer, J.R., Howard, A.D., Schenk, P.M., Beyer, R.A., et al., 2016. The geology of Pluto and Charon through the eyes of New Horizons. Science 351 (6279), 1284–1293. https://doi.org/10.1126/science.aad7055.

Muller, P.M., Sjogren, W.L., 1968. Mascons: Lunar Mass Concentrations. Science 161 (3842), 680–684. https://doi.org/10.1126/SCIENCE.161.3842.680.

Neumann, G.A., Zuber, M.T., Smith, D.E., Lemoine, F.G., 1996. The lunar crust: global structure and signature of major basins. J. Geophys. Res.: Planets 101 (E7), 16841–16863. https://doi.org/10.1029/96JE01246.

Nimmo, F., 2004. Non-Newtonian topographic relaxation on Europa. Icarus 168 (1), 205–208. https://doi.org/10.1016/j.icarus.2003.11.022.
Nimmo, F., McKinnon, W.B., 2021. Geodynamics of Pluto. In: Stern, S.A., Moore, J.M., Grundy, W.M., Young, L.A., Binzel, R.P. (Eds.), The Pluto System after New Horizons. Univ. of Arizona, Tucson, pp. 89–103.
Nimmo, F., Schenk, P., 2006. Normal faulting on Europa: implications for ice shell properties. J. Struct. Geol. 28 (12), 2194–2203.
Nimmo, F., Hamilton, D.P., Mckinnon, W.B., Schenk, P.M., Binzel, R.P., Bierson, C.J., et al., 2016. Reorientation of sputnik Planitia implies a subsurface ocean on Pluto. Nature 540 (7631). https://doi.org/10.1038/nature20148.
Nimmo, F., Umurhan, O., Lisse, C.M., Bierson, C.J., Lauer, T.R., Buie, M.W., et al., 2017. Mean radius and shape of Pluto and Charon from new horizons images. Icarus 287, 12–29.
Potter, R.W.K., Collins, G.S., Kiefer, W.S., McGovern, P.J., Kring, D.A., 2012. Constraining the size of the south pole-Aitken basin impact. Icarus 220 (2), 730–743. https://doi.org/10.1016/J.ICARUS.2012.05.032.
Roberts, J.H., Stickle, A.M., 2021. Breaking the symmetry by breaking the ice shell: an impact origin for the south polar terrain of Enceladus. Icarus 359, 114302.
Schenk, P.M., Beyer, R.A., McKinnon, W.B., Moore, J.M., Spencer, J.R., White, O.L., et al., 2018. Basins, fractures and volcanoes: global cartography and topography of Pluto from new horizons. Icarus 314, 400–433. https://doi.org/10.1016/J.ICARUS.2018.06.008.
Silber, E.A., Johnson, B.C., 2017. Impact crater morphology and the structure of Europa's ice Shell. J. Geophys. Res.: Planets 122 (12), 2685–2701. https://doi.org/10.1002/2017JE005456.
Stern, S.A., Bagenal, F., Ennico, K., Gladstone, G.R., Grundy, W.M., McKinnon, W.B., et al., 2015. The Pluto system: initial results from its exploration by new horizons. Science 350 (6258). https://doi.org/10.1126/science.aad1815.
Trowbridge, A.J., Melosh, H.J., Steckloff, J.K., Freed, A.M., 2016. Vigorous convection as the explanation for Pluto's polygonal terrain. Nature 534. https://doi.org/10.1038/nature18016.
Trowbridge, A.J., Johnson, B.C., Freed, A.M., Melosh, H.J., 2020. Why the lunar south pole-Aitken Basin is not a mascon. Icarus 352, 113995. https://doi.org/10.1016/J.ICARUS.2020.113995.
Turtle, E.P., Melosh, H.J., 1997. Stress and flexural modeling of the Martian lithospheric response to Alba Patera. Icarus 126 (1), 197–211.
Turtle, E.P., Pierazzo, E., 2001. Thickness of a Europan ice shell from impact crater simulations. Science 294 (5545), 1326–1328. https://doi.org/10.1126/science.1062492.
Wünnemann, K., Collins, G.S., Melosh, H.J., 2006. A strain-based porosity model for use in hydrocode simulations of impacts and implications for transient crater growth in porous targets. Icarus 180 (2), 514–527. https://doi.org/10.1016/j.icarus.2005.10.013.
Zahnle, K., Schenk, P., Levison, H., Dones, L., 2003. Cratering rates in the outer solar system. Icarus 163 (2), 263–289. https://doi.org/10.1016/S0019-1035(03)00048-4.